

Multi-level, forming and filament free, bulk switching trilayer RRAM for neuromorphic computing at the edge

Received: 10 October 2023

Accepted: 6 March 2024

Published online: 25 April 2024

 Check for updates

Jaeseoung Park^{1,6}, Ashwani Kumar^{1,6}, Yucheng Zhou¹, Sangheon Oh¹, Jeong-Hoon Kim¹, Yuhan Shi¹, Soumil Jain², Gopabandhu Hota¹, Erbin Qiu³, Amelie L. Nagle⁴, Ivan K. Schuller³, Catherine D. Schuman⁵, Gert Cauwenberghs² & Duygu Kuzum¹✉

CMOS-RRAM integration holds great promise for low energy and high throughput neuromorphic computing. However, most RRAM technologies relying on filamentary switching suffer from variations and noise, leading to computational accuracy loss, increased energy consumption, and overhead by expensive program and verify schemes. We developed a filament-free, bulk switching RRAM technology to address these challenges. We systematically engineered a trilayer metal-oxide stack and investigated the switching characteristics of RRAM with varying thicknesses and oxygen vacancy distributions to achieve reliable bulk switching without any filament formation. We demonstrated bulk switching at megaohm regime with high current non-linearity, up to 100 levels without compliance current. We developed a neuromorphic compute-in-memory platform and showcased edge computing by implementing a spiking neural network for an autonomous navigation/racing task. Our work addresses challenges posed by existing RRAM technologies and paves the way for neuromorphic computing at the edge under strict size, weight, and power constraints.

As the Moore's law is coming to an end due to the limitations of physical scaling of CMOS technology, neuromorphic compute-in-memory (CIM) approaches have attracted huge attention to keep improving computing performance¹. The CIM has the potential to alleviate the von Neumann bottleneck, a limitation in computing performance resulting from significant energy loss and time delays during data transfer between processors and memory units in classical computing systems. While GPUs and tensor processing units excel in parallel computing compared to CPUs, they are still reliant on static random access memory, which demands substantial physical space^{2,3}. Emerging non-volatile memory (eNVM) devices including phase change memory (PCM)⁴, magnetic random access memory (MRAM)⁵,

conductive bridge random access memory (CBRAM)^{6,7}, ferroelectric field effect transistor (FeFET)⁸, resistive random access memory (RRAM)^{9,10}, and memristive synapses based on 2D materials^{11–13} have been extensively studied for physical implementations of neuromorphic CIM platforms. RRAM devices are gaining attention due to their exceptional density, lower fabrication cost, and back-end-of-line (BEOL) compatibility with CMOS technology^{9,14}.

RRAM-based reconfigurable systems hold great promise for low energy and high throughput neuromorphic computing. Neurosynaptic cores constructed by CMOS-RRAM integration have shown dynamically high-performance reconfigurable dataflow and energy efficiency of 74 TMACS/W^{15,16}. However, three major challenges are yet to be addressed

¹Department of Electrical and Computer Engineering, University of California San Diego, La Jolla, CA, USA. ²Department of Bioengineering, University of California San Diego, La Jolla, CA, USA. ³Department of Physics, University of California San Diego, La Jolla, CA, USA. ⁴Department of Computer Science, Massachusetts Institute of Technology, Cambridge, MA, USA. ⁵Department of Electrical Engineering and Computer Science, University of Tennessee, Knoxville, TN, USA. ⁶These authors contributed equally: Jaeseoung Park, Ashwani Kumar. ✉ e-mail: dkuzum@ucsd.edu

to scale CMOS-RRAM based accelerators and achieve energy-efficient dynamic on-chip learning with RRAM crossbar arrays: (i) Most of the RRAM devices rely on filamentary switching, which suffers from extensive variations and noise leading to computational accuracy loss and increased energy consumption¹⁷. Programming RRAM into multi-level resistance states requires expensive read and verify programming schemes, unsuitable for on-chip training^{18,19}. (ii) Low ON-state resistance of filamentary RRAM increases the power consumption due to high current read and write operations. As the resistance approaches the interconnect resistance²⁰, it constrains the array size and parallel multiply & accumulate (MAC) operations. (iii) Filamentary RRAM requires high forming voltages to generate a conductive filament, that is not compatible with advanced CMOS technology nodes. To address all these challenges, here, we demonstrate systematic engineering of a trilayer metal-oxide bulk RRAM stack and investigate the switching characteristics of RRAM devices with varying thicknesses and V_O distributions across the trilayer. Sputtered porous TiO_x layer facilitates modulation of V_O distribution in the switching layer without forming V_O filaments (Fig. 1a), enabling bulk switching operations in the megaohm (M Ω) range, achieving high current nonlinearity, and programming up to 100 levels without the need for compliance current. Highly linear MVMs are achieved by using the row-differential scheme instead of non-differential scheme in fabricated bulk RRAM crossbars²¹. We employ the fabricated RRAM crossbars to perform control for an autonomous navigation/racing task using a spiking neural network (SNN) model, demonstrating compatibility for neuromorphic computing at the edge applications. Our work tackles the challenges presented by current filamentary RRAM technologies, clearing a path for neuromorphic computing at the edge while adhering to stringent size, weight, and power constraints.

Results

Optimization of trilayer bulk RRAM stack

To systematically investigate switching characteristics of RRAM devices based on multi-layer stacks, we fabricated RRAM devices in four

different switching layer ($Al_2O_3/TiO_2/TiO_x$) configurations (Table 1). Our detailed fabrication process is explained in the methods. All samples include 3 nm Al_2O_3 as a high bandgap tunnel barrier ($E_g \sim 9.0$ eV) layer to limit the current and provide I-V nonlinearity through tunneling. For S1 and S2, ALD TiO_2 layers ($S1 = 20$ nm, $S2 = 40$ nm) were deposited without breaking the vacuum. S3 and S4 have 3 nm ALD TiO_2 and sputtered TiO_x layers ($S3 = 6.5$ nm, $S4 = 40$ nm) with varying oxygen stoichiometry (Fig. 1a). As shown in the plane-view and cross-sectional SEM images, 16×16 crossbar arrays were fabricated using a via-hole structure design (Fig. 1b–d). The via-hole structure was chosen to achieve uniform and reliable device switching instead of simple crossbar structure. The via-hole design with 150 nm thick plasma-enhanced chemical vapor deposition (PECVD) SiO_2 insulator eliminates the edge effects due to high-field corners or sidewalls²². In addition, all steps of the fabrication process have low thermal budget ($T < 300$ °C) which is perfectly compatible with CMOS BEOL integration process.

We first tested DC switching characteristics for all samples. Both S1 (Fig. 1e, $R_{on} = 150$ Ω , $R_{off} = 400$ k Ω) and S2 (Fig. 1f, $R_{on} = 3$ k Ω , $R_{off} = 2$ G Ω) exhibit only filamentary switching with significant variations in set/reset voltages in consistent with the previous research on the filamentary RRAM using Al_2O_3/TiO_{2-x} stacks⁹. The high OFF-state resistance of S2 is due to thicker TiO_2 layer. A 200 μ A compliance current is necessary to prevent permanent breakdown during DC set process for both devices. Although the filamentary RRAM shows resistance switching behavior, these devices suffer from highly non-uniform switching characteristics due to the stochastic nature of filament formation and rupture¹⁷. The low ON-state resistance of the filamentary RRAM also increases the power consumption due to high energy read and write operations. In addition, the abrupt resistance jumps during the set and reset processes are not suitable for continuous synaptic weight updates during online learning where the multi-level conductance update is needed. RRAM devices including sputtered TiO_2 (S3) or TiO_x (S4) layer exhibit bulk switching characteristics (Fig. 1g, h). Surprisingly, S3 shows both filamentary and bulk

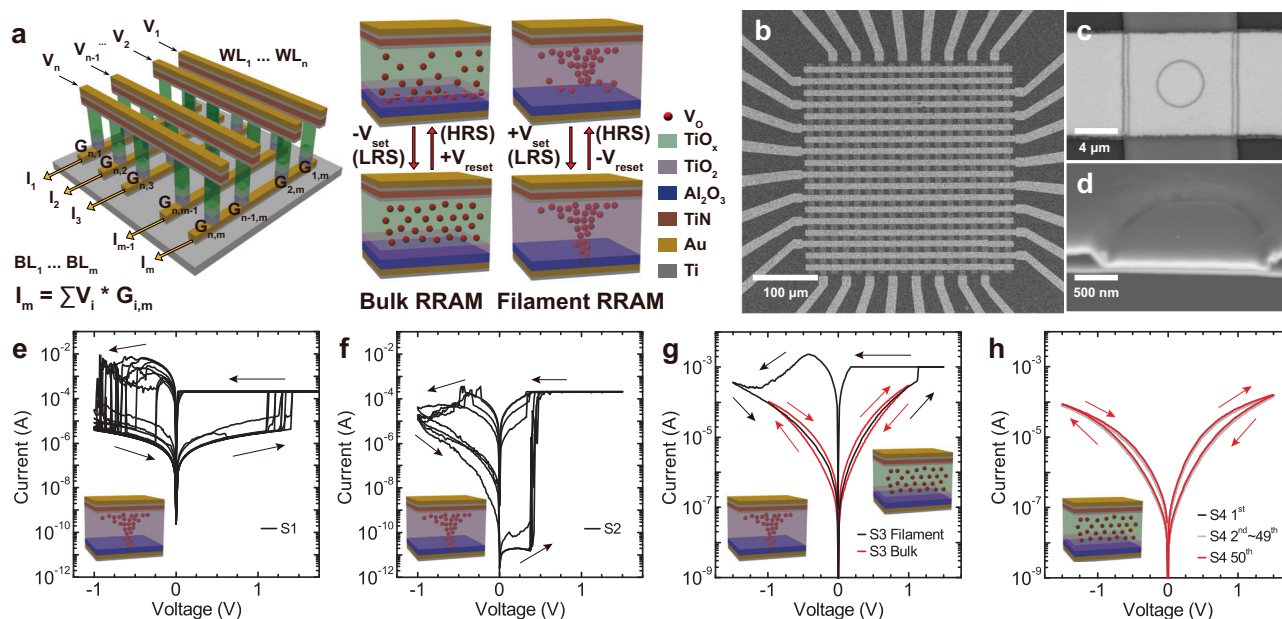


Fig. 1 | RRAM device stack and DC I-V switching characterization. **a** Illustration of fabricated RRAM device stack and crossbar arrays. Bulk and filamentary RRAM switching mechanisms are compared. For bulk switching, the distribution of oxygen vacancies (V_O) is modulated between TiO_x and TiO_2 layers. For filamentary switching, the V_O filament formation and rupture occur near the bottom electrode. Scanning Electron Microscopy (SEM) images of fabricated **b** 16×16 crossbar array **c** single trilayer RRAM device, and **d** cross-section of a half-cut RRAM device.

Filamentary switching characteristics of **e** S1 and **f** S2. **g** Coexistence of filamentary and bulk switching in S3. They show the opposite polarity due to the different resistance-switching mechanisms. Black arrows show the polarity of filamentary switching, while red arrows show polarity of bulk switching. **h** Bulk RRAM DC I-V characteristics of S4 without forming filaments. 50 cycles of DC sweeps perfectly overlap, showing highly uniform bulk switching.

switching with a transition from bulk switching to filamentary switching as DC sweep range is increased from 1 V to 1.5 V. In high voltage DC sweep range ($|V| < 1.5$ V) where filamentary switching is observed, it follows the same switching polarity (a positive set and negative reset voltage) as S1 and S2 filamentary RRAM devices ($R_{\text{on}} = 200 \Omega$, $R_{\text{off}} = 145 \text{ k}\Omega$). In low voltage DC sweep range ($|V| < 1$ V) where bulk switching dominates, it demonstrates gradual resistance change during DC sweep without any sudden resistance jumps that are observed in filamentary switching ($R_{\text{on}} = 76 \text{ k}\Omega$, $R_{\text{off}} = 180 \text{ k}\Omega$). Switching direction for bulk switching (a negative voltage set and a positive voltage reset) show opposite polarity to filamentary switching. Although both filamentary and bulk switching are observed in different voltage regimes and the opposite polarity, coexistence of both mechanisms is not desirable for reliable synaptic weight updates²³. For the RRAM devices with a thicker and V_{O} -rich sputtered TiO_x layer (S4), only bulk switching behavior is observed without any filament formation. S4 exhibits, highly reliable bulk switching behavior with excellent uniformity over 50 DC cycles (Fig. 1h, $R_{\text{on}} = 410 \text{ k}\Omega$, $R_{\text{off}} = 1 \text{ M}\Omega$). Furthermore, the bulk switching for S4 exists in the $\text{M}\Omega$ resistance range in contrast to bulk switching occurring $\sim 100 \text{ k}\Omega$ for S3. Therefore, we decided to further investigate switching characteristics and multi-level resistance states for the trilayer bulk RRAM (S4) and chose it for neuromorphic computing with the crossbar array demonstrations.

To analyze trilayer structure of the bulk switching RRAM, the transmission electron microscopy (TEM) and scanning transmission electron microscopy - electron energy loss spectroscopy (STEM-EELS) analyses were performed (Fig. 2). We estimated the composition of Ti

metal layer as $\text{TiO}_{1.2}$ based on the composition analysis. The top Ti metal layer scavenges the oxygen from the sputtered TiO_x layer due to the lower chemical potential of oxygen in Ti suboxides than that in TiO_2 ²⁴. There are previous studies that exploit Ti as a scavenging layer to reduce underlying oxide layers^{25,26}. For example, for the Nb-based selector device fabrication, Ti metal plays an important role in stabilizing the underlying NbO_2 selector layer without further oxidation to the thermally stable Nb_2O_5 composition. The Ti metal also reduces Hf-based oxides to induce oxygen vacancy defects in it so that the RRAM device can form the filaments at the lower set voltage. The ALD TiO_2 layer has darker contrast in bright field-TEM image, confirming higher atomic density than the TiO_x layer (Fig. 2a). STEM-EELS line-scan profile shows lower oxygen concentration in TiO_x layer than ALD TiO_2 layer (Fig. 2b). Furthermore, STEM-EELS composition map (Fig. 2c) shows nm-scale dark areas only in the sputtered TiO_x layer pointing to a porous structure. To further analyze the crystal structure and film density, grazing incidence X-ray diffraction (GIXRD) and X-ray reflection (XRR) measurements were conducted (Supplementary Fig. S1). 30 nm ALD TiO_2 layer shows crystalline anatase phase while sputtered TiO_x films show an amorphous phase. The grain boundaries are well known to be the high diffusivity paths of small ions such as oxygens or hydrogens^{27,28}. Especially in polycrystalline filament RRAM devices, the grain boundaries acts an important role in charge transport and V_{O} accumulation and diffusion²⁹. Due to these diffusivity paths, filament formation and rupture easily occur in the filamentary RRAM devices (S1 and S2). In the amorphous phase, however, there are no high diffusivity paths for V_{O} , so the filament formation can be successfully suppressed. XRR measurements show that the critical angle of sputtered TiO_x layer (0.52°) is smaller than ALD TiO_2 layer (0.55°), suggesting that the film mass density is smaller for the sputtered TiO_x layer. The distribution of V_{O} defects is modulated by the external electric field in a whole switching layer rather than forming a locally accumulated V_{O} filaments, so that we can achieve bulk switching behavior.

Table 1 | Four different multilayer stacks are fabricated (S1–S4). Only the trilayer with a sputtered TiO_x layer (S4) shows stable bulk switching characteristics without filament formation

Sample	Oxide stack	Dominating switching
S1	ALD $\text{Al}_2\text{O}_3/\text{TiO}_2$ (3 nm/20 nm)	Filamentary
S2	ALD $\text{Al}_2\text{O}_3/\text{TiO}_2$ (3 nm/40 nm)	Filamentary
S3	ALD $\text{Al}_2\text{O}_3/\text{TiO}_2$ (3 nm/3 nm) / Sputter TiO_2 (6.5 nm)	Filamentary/Bulk
S4	ALD $\text{Al}_2\text{O}_3/\text{TiO}_2$ (3 nm/3 nm) / Sputter TiO_x (40 nm)	Bulk

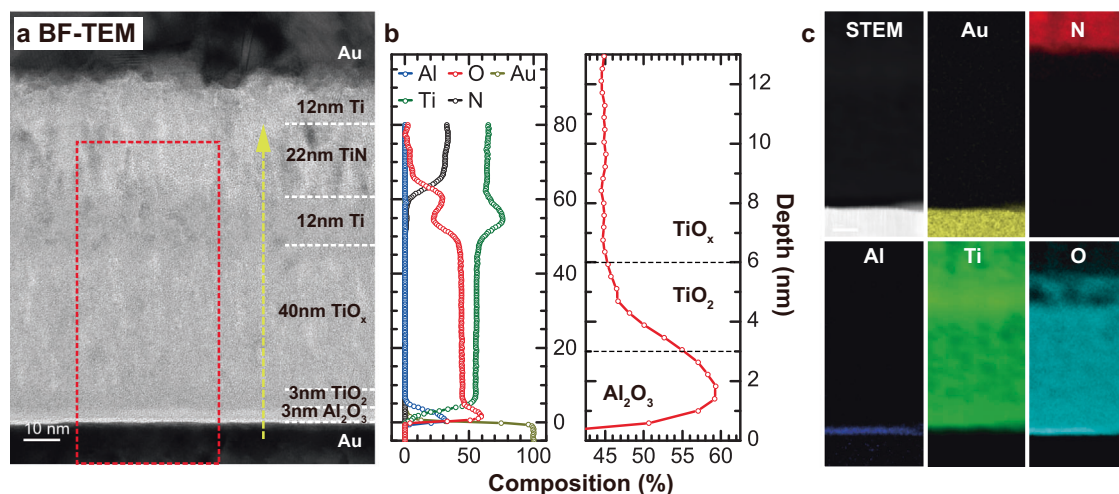


Fig. 2 | Cross-sectional analysis of bulk RRAM device. a Cross-sectional bright-field Transmission Electron Microscopy (TEM) image of trilayer bulk RRAM. The bright contrast of TiO_x suggests a porous structure for the layer. **b** Atomic concentration profile measured by Scanning Transmission Electron Microscopy – Electron Energy Loss Spectroscopy (STEM-EELS) along the yellow arrow. All

interfaces were determined based on the ion concentration and contrast in TEM image. The sputtered TiO_x layer shows a smaller oxygen concentration which is lower than ALD TiO_2 layer due to the V_{O} in the layer. **c** STEM-EELS mapping of red dotted box region in **a**.

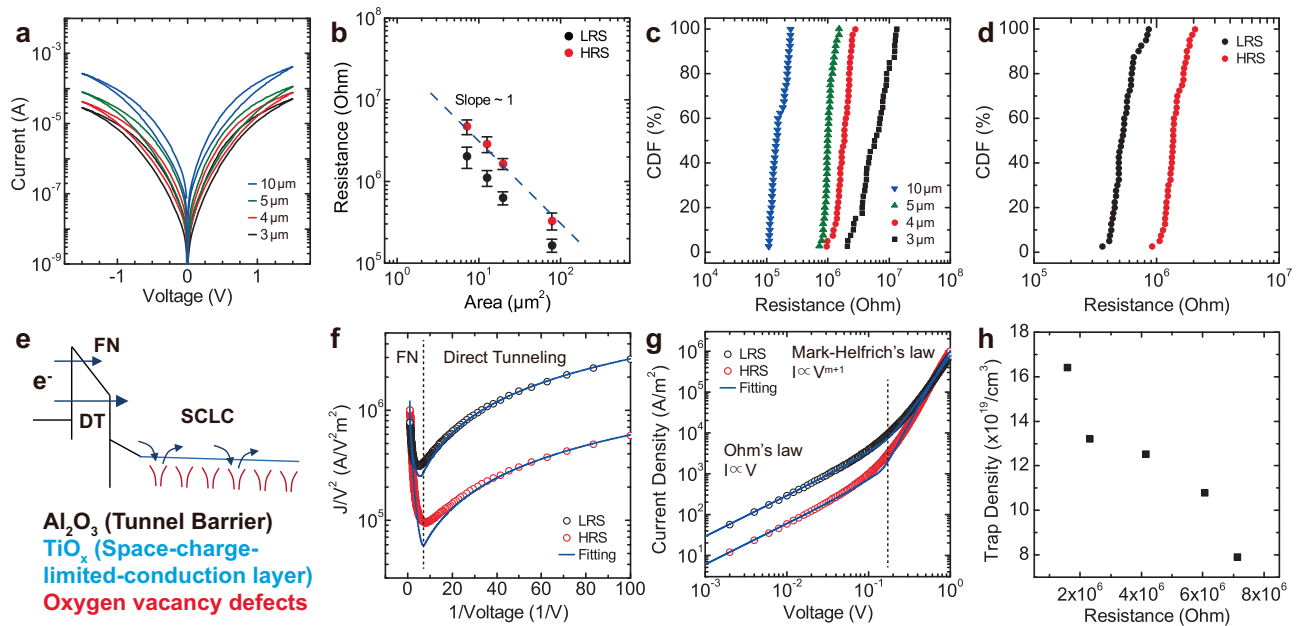


Fig. 3 | Electrical DC characterization of bulk RRAM devices. **a** DC I-V switching curves of trilayer bulk RRAM with different diameter cells from 3 to 10 μm . **b** Double log plot of resistance vs. cell area. Area-scaling behavior with a slope of 1 suggests bulk switching of RRAM devices. Each size cell data is collected from 40 different devices measured at $V_{\text{read}} = 0.1\text{ V}$. **c** Cumulative distribution function (CDF) of bulk RRAM pristine resistance in different size cells. **d** CDF of LRS and HRS states programmed with DC sweep using bulk RRAM $5\mu\text{m}$ devices. **e** Band diagram of trilayer bulk RRAM. Al_2O_3 3 nm wide gap layer acts as a tunneling barrier where

the direct/Fowler-Nordheim (FN) tunneling happen at small/large voltage region. In the TiO_x layer, space-charge-limited-conduction (SCLC) occurs due to deep-level V_O defects. **f** $\log(I/V^2)$ vs. $1/V$ curves of high resistance state (HRS) and low resistance state (LRS). Both states show similar conduction mechanisms. **g** $\log J - \log V$ plot of LRS and HRS states. In low voltage regime, current density follows the Ohm's law ($J \propto V$), while it follows the Mark-Helrich's law ($J \propto V^{m+1}$) in high voltage regime. **h** Trap density (N_t) vs. device resistance curve. N_t is achieved by the fitting the experimentally measured data with our electrical conduction model.

scales with the area for both high resistance (HRS) and low resistance states (LRS) (Fig. 3b), suggesting bulk switching^{23,30}. In the filamentary RRAM, both HRS and LRS resistances are independent on the device area because the resistance depends on the width and conductivity of the filament that can only be modulated by the compliance current during the SET process³¹. The device-to-device (D2D) variations of pristine, HRS, and LRS states show tight distributions in M Ω regime (Fig. 3c, d), addressing the high variability issue of filamentary RRAM devices. Perfectly overlapping DC sweeps over 50 cycles (Fig. 1h) suggest that the trilayer bulk RRAM exhibits minimal cycle-to-cycle variation.

We systematically studied the conduction mechanism of trilayer bulk RRAM by fitting DC I-V characteristics with direct tunneling, Fowler-Nordheim (FN) tunneling and space-charge-limited conduction (SCLC) models in both HRS and LRS (Fig. 3e–h). To investigate the conduction mechanism in the bulk RRAM devices, the I-V characteristics are plotted in a $\log(I/V^2)$ vs. $1/V$ form (Fig. 3f). In this plot, there are two different voltage regime where the direct tunneling and Fowler-Nordheim (FN) tunneling dominate by the following relations (Direct tunneling, $I \propto V$ /FN tunneling, $I \propto V^2 \cdot \exp(-1/V)$)^{32,33}. We developed a model explaining current conduction in our bulk RRAM devices (Supplementary note 1) and fitted to experimental results shown in Fig. 3f, g. To further validate our model, we performed temperature-dependent I-V measurements on our bulk RRAM devices and fitted the measurement results to our model (Supplementary Fig. S2). Our model based on direct tunneling, Fowler-Nordheim tunneling, and SCLC shows great agreement with the current voltage characteristics at all temperatures and voltage ranges.

In the low voltage regime ($V < 0.06\text{ V}$), the current of both HRS and LRS states are linear to the voltage, meaning that the direct tunneling is the dominant conduction mechanism. In the high voltage regime ($V > 0.5\text{ V}$), however, the $\log(I/V^2)$ is linear to the $1/V$, where the FN tunneling becomes dominant. These tunneling conduction occur

through the high band gap Al_2O_3 layer which provides the M Ω -level resistance switching and high nonlinearity ($I_V/I_{0.5V} = 15$ ($V = 1.5\text{ V}$)) of I-V curves³⁴. Both HRS and LRS states of bulk RRAM devices follow the same conduction mechanism, whereas the filamentary RRAM or CBRAM would show ohmic conduction in LRS states because current conduction occurs through the V_O or metal cation filaments^{35,36}. To study the switching mechanism, the double-log plot of I-V curves were fitted with the SCLC theory^{37–39} (Fig. 3g). In the low voltage regime, the double-log I-V curves follows a linear relationship due to the dominance of the electron drift across TiO_x layer ($I \propto V$). In the high voltage regime, they follow a power dependency on voltage due to the trap-limited conduction through the V_O deep defects in the sputtered TiO_x layer ($I \propto V^{m+1}$, $m = T_c/T$, T_c is the characteristic temperature). Experimental I-V measurement data were fitted using our model (Supplementary note 1), and the trap density (N_t) was extracted. Figure 3h shows that the trap density is decreased as the device resistance is increased.

Bulk switching can be better understood by reviewing filamentary RRAM first. In the filamentary RRAM, V_O defects are well known to be mobile with external electrical and thermal stimuli⁴⁰. Filamentary RRAM needs an initial electroforming step which forms the V_O defect filaments between two electrodes. Once the filaments are formed bipolar switching takes place due to the forming and rupturing of the filaments. Meanwhile, the grain boundaries are well known to be the high diffusivity paths of small ions such as oxygens or hydrogens in crystalline oxides^{27,28}. Especially for our polycrystalline filamentary RRAM devices (S1, S2), the grain boundaries play an important role in charge transport and V_O accumulation and diffusion. Due to these diffusivity paths, filament formation and rupture easily occur in the filamentary RRAM devices.

In our bulk RRAM devices, we deposited an amorphous, porous, and V_O -rich thick TiO_x layer instead of having a crystalline ALD TiO_2 layer. Due to the absence of fast diffusion paths or accumulation

sites for V_O defects in the amorphous phase, the V_O defects are not clustered in specific locations that facilitate filament formation. The filament formation is effectively suppressed in an amorphous layer as compared to the crystalline phase in RRAM devices⁴¹. V_O defects will drift homogeneously throughout the entire area of the layer rather than forming defects-clustered filaments, following the direction of the electric field, enabling bulk switching instead of filamentary switching. When a positive voltage is applied to the top electrode, the V_O are pushed downwards towards the bottom electrode and the V_O concentration in the TiO_x layer is reduced. Space-charge-limited-conduction (SCLC) dominates the conduction in the TiO_x layer. Since the V_O concentration in the TiO_x layer is reduced, the SCLC current decreases confirming that the device is reset to a higher resistance state. Our fitting results shown in Fig. 3g and reduced trap density shown in Fig. 3h confirms this model for the bulk switching mechanism. The bulk switching shows the opposite polarity to the filamentary switching consistent with other previous reports^{23,42}.

The ability to perform analog weight updates is a crucial feature in synaptic devices for efficient implementation of learning and inference in neuromorphic computing applications. Analog weight update is the most important property in synaptic devices to achieve successful neuromorphic computing applications. The filamentary RRAM shows abrupt resistance change so that they have been mainly employed for binary or low-precision implementation of neural network weights. Programming filamentary RRAM devices into discrete conductance states require extensive number of program and verify operations, not suitable for online learning applications³⁰. In contrast, for the bulk RRAM devices, it is easier to achieve gradual weight updates. We first investigated gradual weight updates using identical pulses in two different conductance regimes; $-0.8 \mu\text{s}$ and $-0.12 \mu\text{s}$. 32-states are achieved by applying of identical set and reset pulses for both conductance regimes (Fig. 4a, b). The long-term potentiation (LTP) and the long-term depression (LTD) curves show gradual conductance change ($V_{\text{read}} = 0.1 \text{ V}$). We also implemented an incremental pulse scheme. We optimized the incremental pulse scheme to have linear LTP and LTD curves with a higher dynamic range and larger number of states (Fig. 4c). Figure 4d, e shows the gradual current increase/decrease during the transient set (-2.0 V)/reset ($+1.5 \text{ V}$) pulses. We quantitatively analyzed the device non-linearity and found that incremental pulse scheme can improve non-linearity (Supplementary Fig. S3, Supplementary note 2). The non-linearity could be improved by further optimizing the pulse amplitude and width for potentiation and depression. To compensate for the non-linearity effect in hardware implementation of neural networks, we previously developed the adaptive quantization method, which maps neural network weights onto the device conductances based on the distribution and relative importance of the weights⁴³. Various other nonuniform quantization methods have also been adopted by the broader neural networks community to improve efficiency of neural networks^{44,45}. Based on all the pulse measurement results, the trilayer RRAM devices show gradual conductance switching in $\text{M}\Omega$ regime that can overcome the drawbacks of filamentary RRAM devices which show binary resistance states in $\text{k}\Omega$ regime. We investigated cycling properties of our trilayer bulk RRAM devices by performing endurance measurements based on pulse programming. As shown in Supplementary Fig. S4a, the pulse endurance test results exhibit stable weight modulation until 2×10^5 cycles under set/reset pulses (Set: $-2.0 \text{ V } 5 \text{ ms}$ /Reset: $1.0 \text{ V } 5 \text{ ms}$). We also extracted the variations (σ) from the endurance cycling tests and the variations were about 1% which is enough to differentiate the different conductance states. Read disturbance is tested up to 200k cycles and they show no degradation in device characteristics due to uniform and stable bulk RRAM switching (Supplementary Fig. S4).

Hardware SNN implementation with RRAM crossbars

For the hardware implementation of neural networks, we first investigated the effect of ON and OFF state resistances (R_{ON} and R_{OFF}) on the read and write operations across crossbar arrays using circuit simulations (HSPICE). Supplementary Fig. S5a shows that for $R_{\text{OFF}} < 10 \text{ M}\Omega$, the read margin significantly degrades as the array size increases. For the write operation, the voltage across individual RRAM cells decreases with R_{ON} (Supplementary Fig. S5b). These results indicate the importance of $\text{M}\Omega$ range resistance to maintain read and write accuracy for selector-less crossbars. Although $\text{M}\Omega$ resistance and non-linearity of trilayer RRAM are great for reliable crossbar operation, a small dynamic range ($R_{\text{ON}}/R_{\text{OFF}} \sim 2.5$) is a limiting factor. To address that, we employed a row-differential encoding scheme (Fig. 5a), where two RRAMs represent positive and negative weights by utilizing opposite voltage polarity, i.e., $V_{\text{WL}+} = V_{\text{ref}} + V_{\text{READ}}$, $V_{\text{WL}-} = V_{\text{ref}} - V_{\text{READ}}$. The differential conductance 'Diff_G' given by $G^+ - G^-$, represents both positive and negative weights. For the differential read of multi-level RRAM, the effective dynamic range depends on the minimum achievable conductance difference ($\text{Diff_G}_{\text{min}}$) as in equation ' $2(G_{\text{max}} - G_{\text{min}})/\text{Diff_G}_{\text{min}}$ ' (Fig. 5a). It results in a significantly higher dynamic range (~ 170) compared to the non-differential single RRAM scheme (Fig. 5b) due to the small ' $\text{Diff_G}_{\text{min}}$ ', helping with mapping a wider range of real-valued weights. For hardware implementation with RRAM crossbar arrays, we developed a neuromorphic compute-in-memory platform (Fig. 5d). It utilizes a switched capacitor voltage-sensing circuit to avoid the need for current-sensing schemes relying on high-power large-area transimpedance amplifiers (Fig. 5e, f)⁴⁶. We performed read (Fig. 5g) and MVM computations on the trilayer RRAM crossbar and demonstrated the differential scheme can achieve highly linear MVM computation.

For neuromorphic computing at the edge with trilayer bulk RRAM crossbars, we implemented an SNN trained using Evolutionary Optimization for Neuromorphic Systems (EONS) algorithm⁴⁷. In EONS algorithm, randomly generated populations are used as initial seeds for neural network optimizations. The fitness score, a criterion to measure neural network accuracy is assessed in each neural network during the evaluation step. Then, the selected networks through the tournament methods are used to perform reproduction steps where various operators occur (e.g., duplication, crossover, and mutation). In this research, the SNN was specifically trained for a small-scale autonomous racing task⁴⁸ using LIDAR sensor data as the input and producing speed and steering angle as the outputs. For the evolutionary training, the fitness function was defined to evaluate the spiking neural network and to encourage behaviors for completing the task without colliding with a wall⁴⁸. The SNN was trained on 5 Formula-1 tracks and tested on an additional 15 tracks (representative tracks are shown in Fig. 6a) (https://github.com/fltenth/fltenth_racetracks), performing pruning after the training. The pruned SNN consists of 14 input neurons and 30 output neurons including recurrent connectivity across and within the layers (Fig. 6b). For the hardware demo, SNN weights were quantized into 4-bit precision and mapped onto RRAM arrays according to the row-differential scheme. Experimentally mapped weights onto the crossbar show high consistency with the ideal (target) weight map (Fig. 6c). Figure 6e, f shows steering angle and speed calculated based on experimental RRAM weights in comparison to software simulation during autonomous navigation testing of the Catalunya map. Quantitative comparison of speed and steering angle computations during navigation through all 15 racetracks show great agreement with the ideal software simulation of the SNN (Fig. 6d).

Furthermore, to compare our work to other technologies (i.e., $\text{HfO}_x\text{:Si}$ ⁴⁹, $\text{HfO}_x\text{:TaO}_y$ ¹⁵, and $\text{Al}_2\text{O}_3\text{/TiO}_2$ ⁹) at the architecture level, we simulated the energy consumption by the SNN model trained for the same navigation tasks while implementing the required synaptic weights using these different RRAM technologies. Supplementary Figs. S6 and S7 show total energy needed to navigate all racetracks and individual

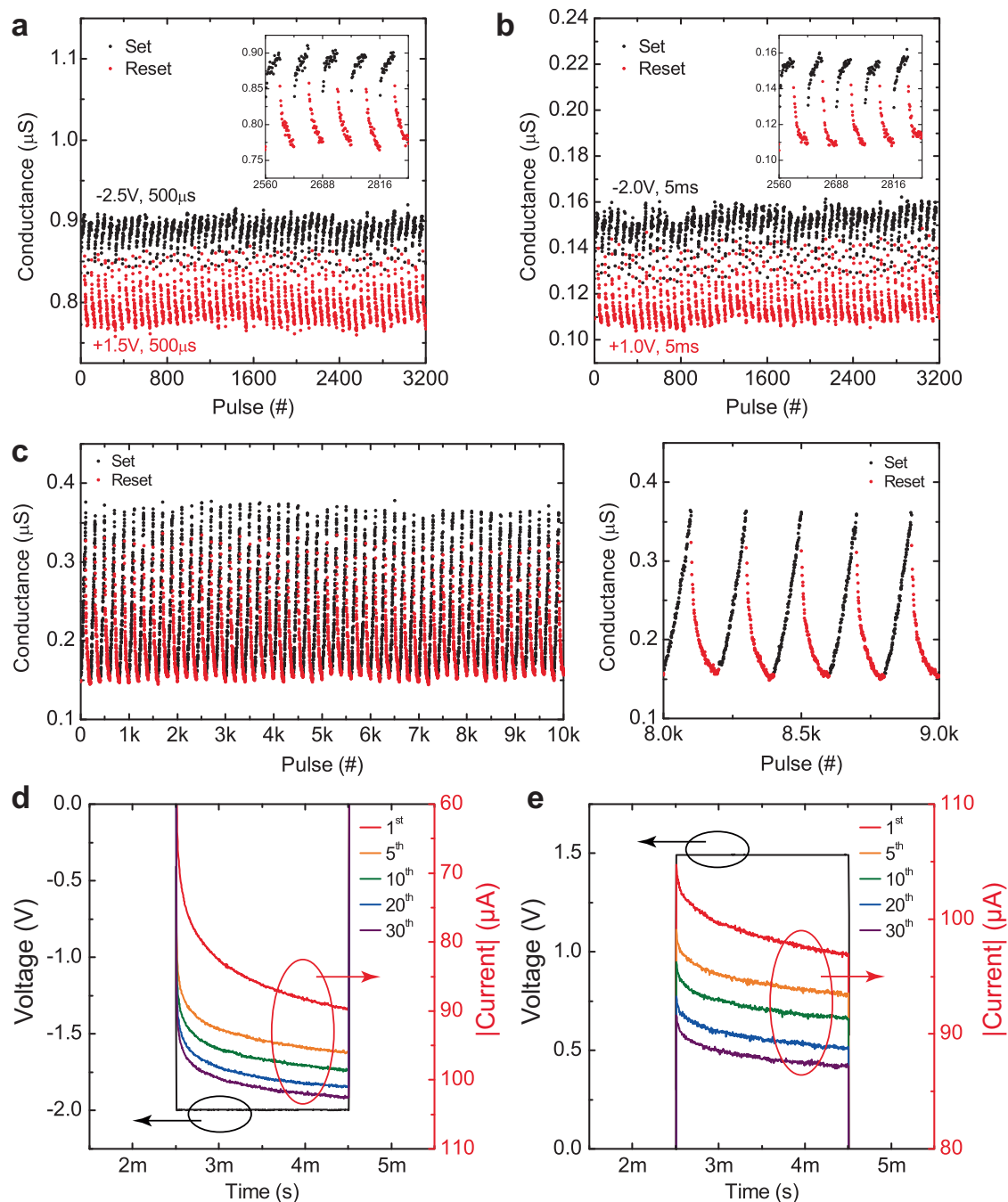


Fig. 4 | Multilevel gradual switching characteristics of the bulk RRAM devices using pulse measurements. **a** Multilevel switching using an identical pulse scheme for 32 different states. Set: -2.5V , $500\mu\text{s}$ /Reset: $+1.5\text{V}$, $500\mu\text{s}$. **b** Multilevel switching using an identical pulse scheme for 32 different states. Set: -2.0V , 5ms /Reset: $+1.0\text{V}$, 5ms . **c** Multilevel switching using an incremental pulse scheme for

100 states. Set: -0.8V to -2.78V (-20mV step)/Reset: $+0.3\text{V}$ to $+0.993\text{V}$ ($+7\text{mV}$ step). The transient current measurements using identical pulses **d** set (-2V) and **e** reset ($+1.5\text{V}$) operations showing multi-level bulk switching without any abrupt current jumps (no filaments).

racetracks, respectively. Our results suggest that our trilayer bulk RRAM substantially (more than order of two) reduces energy consumed by the synaptic arrays in comparisons to other RRAM technologies.

Discussion

In this work, we successfully demonstrated a forming-free bulk switching RRAM technology by engineering a trilayer metal-oxide stack. We systematically optimized the trilayer oxide stacks which consist of high bandgap tunneling barrier (Al_2O_3) and different stoichiometric TiO_2 and TiO_x layers. Due to the highly porous and amorphous TiO_x layer, V_O filament formation was effectively suppressed,

whereas the crystalline TiO_2 layer showed filamentary switching characteristics. The thickness of the Al_2O_3 tunnel barrier was chosen as $\sim 3\text{nm}$ to set the device resistance to $-\text{M}\Omega$ regime (Supplementary Note 3, Supplementary Fig. S8a). Thick TiO_x layer was needed to reduce the electric field across the V_O -rich SCLC layer so that facile filament formation due to drift and clustering of V_O could be prevented (Supplementary Fig. S8b). We achieved multi-level, uniform bulk switching in $\text{M}\Omega$ regime without a compliance current in the bulk RRAM devices.

We benchmarked our bulk RRAM device against different RRAM technologies and showed the advantages on several metrics, i.e.,

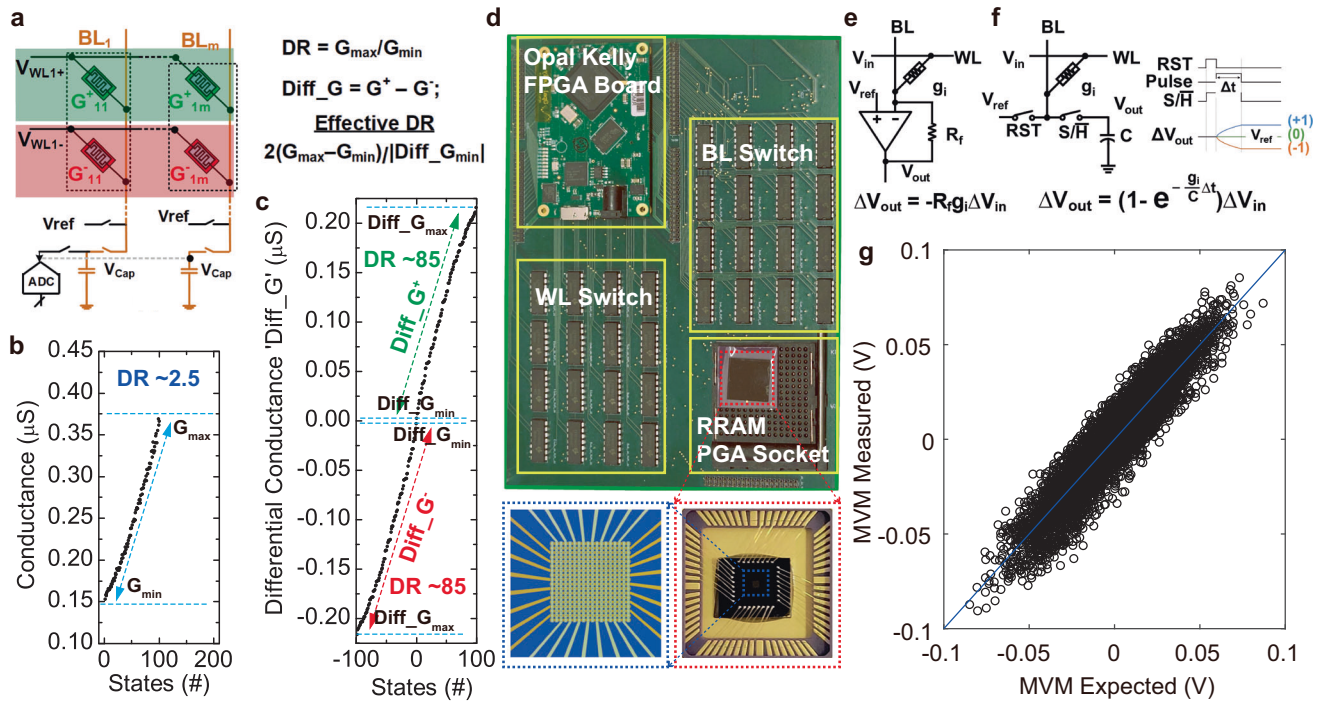


Fig. 5 | Row-differential voltage sensing using neuromorphic compute-in-memory platform with packaged bulk RRAM crossbar. a Row-differential scheme. Two RRAMs sharing the same column represent positive and negative weights by applying opposite polarity voltage to respective WLs. **b** Dynamic range for switching for bulk RRAM. **c** Dynamic range enhancement using the row-differential scheme. For 100 levels, the row-differential scheme can increase the

effective dynamic range up to ~ 170 . **d** Photograph of neuromorphic compute-in-memory board with packaged bulk RRAM crossbar. **e** Conventional current sensing using transimpedance amplifier. **f** Switched-capacitor voltage-sensing circuit to achieve higher energy efficiency. **g** Measured and expected MVM outputs for the differential encoding.

forming free, multilevel, switching voltages, energy consumption, BEOL compatibility, and robustness (Supplementary Table S2, Supplementary note 4). The key figures of merit of our bulk RRAM technology can be summarized as follows; forming-free operation, CMOS BEOL compatibility, high R_{on} and R_{off} that enables reliable read and write in large scale crossbar arrays and low energy operation, low switching voltages, high number of conductance states, endurance comparable to other RRAM technologies, and much lower total read energy.

Next step for the bulk RRAM technology is scaling device dimensions to the nm regime. One potential concern could be variability for nanoscale devices. For memory technologies, the root cause of the higher variability of characteristics due to cell scaling is related to the number of charged carriers or particles. For instance, the charge trap memory with 10-nm technology node can store only 10 electrons per device which cause severe variability issues in the device characteristics⁵⁰. Therefore, we established a conduction model for our bulk RRAM devices to extract the number of oxygen vacancy defects, which demonstrates 1.26×10^{26} V_{O} defects/ m^3 in the layer. When we assume the device scales down to 20 nm size with 40 nm thickness, ~ 2000 V_{O} defects exist in a single device. The order of V_{O} defects in a single cell is more than 3 orders higher than the number of trapped electrons in a 10 nm tech node flash memory devices, so variability related to the low number of defects is not expected to be a major problem for our bulk RRAM devices. In addition, the high variability in the conventional RRAM devices come from the stochastic nature of the filaments. Since both set and reset processes are determined by the stochastic movement of atoms in the switching oxides, the device-to-device and cycle-to-cycle variability have been a main problem of filamentary RRAM devices. In our bulk RRAM devices, resistance is modulated by controlling the defect concentration in the switching layer so that the variability problem of stochastic 1D

filaments can be resolved. In addition, the previous study about bulk RRAM devices demonstrated uniform resistive switching characteristics when the device is scaled down to $60 \times 60 \text{ nm}^2$ ²³. Finally, for the scaled bulk RRAM devices, the tunnel oxide and the TiO_x switching layer thicknesses could be reoptimized to match $\text{M}\Omega$ resistance level.

In this work, we developed a neuromorphic CIM platform using bulk RRAM crossbars by combining energy-efficient switched-capacitor voltage sensing circuits with differential encoding of weights. The row-differential weight encoding enabled to increase dynamic range of bulk RRAM devices as well as to give high-accuracy MVM operations. We successfully mapped weights of SNN network for autonomous navigation/racing tasks on Formula-1 racetracks onto bulk RRAM crossbars using the row-differential weight encoding scheme. The fitness score of weight maps on crossbars hardware showed good agreement with ideal software simulation results, suggesting a computational capability of bulk RRAM crossbars. Our work addresses the problems of the filamentary RRAMs and offers a promising pathway towards energy-efficient dynamic on-chip learning with RRAM crossbars.

Methods

Bulk RRAM fabrication and packaging crossbars

Ti (12 nm)/Au (100 nm) bottom electrode was deposited by the sputtering on a 4-inch SiO_2 (300 nm)/Si wafer with bilayer lift-off process (LOR5B and AZ1512). Plasma-enhanced chemical vapor deposition (PECVD) SiO_2 (150 nm) layer was deposited as an insulating interlayer dielectric layer. Various via-hole sizes (Diameter: $3 \mu\text{m}$ to $10 \mu\text{m}$) were patterned with maskless photolithography and inductively coupled plasma etching process with CF_4 atmosphere. The $\text{Al}_2\text{O}_3/\text{TiO}_2$ (3 nm/3 nm) atomic layer deposition (ALD) layer was deposited with trimethyl aluminum (TMA) and titanium chloride (TiCl_4) precursor and water oxidant without breaking vacuum. The sputtered TiO_x layer was

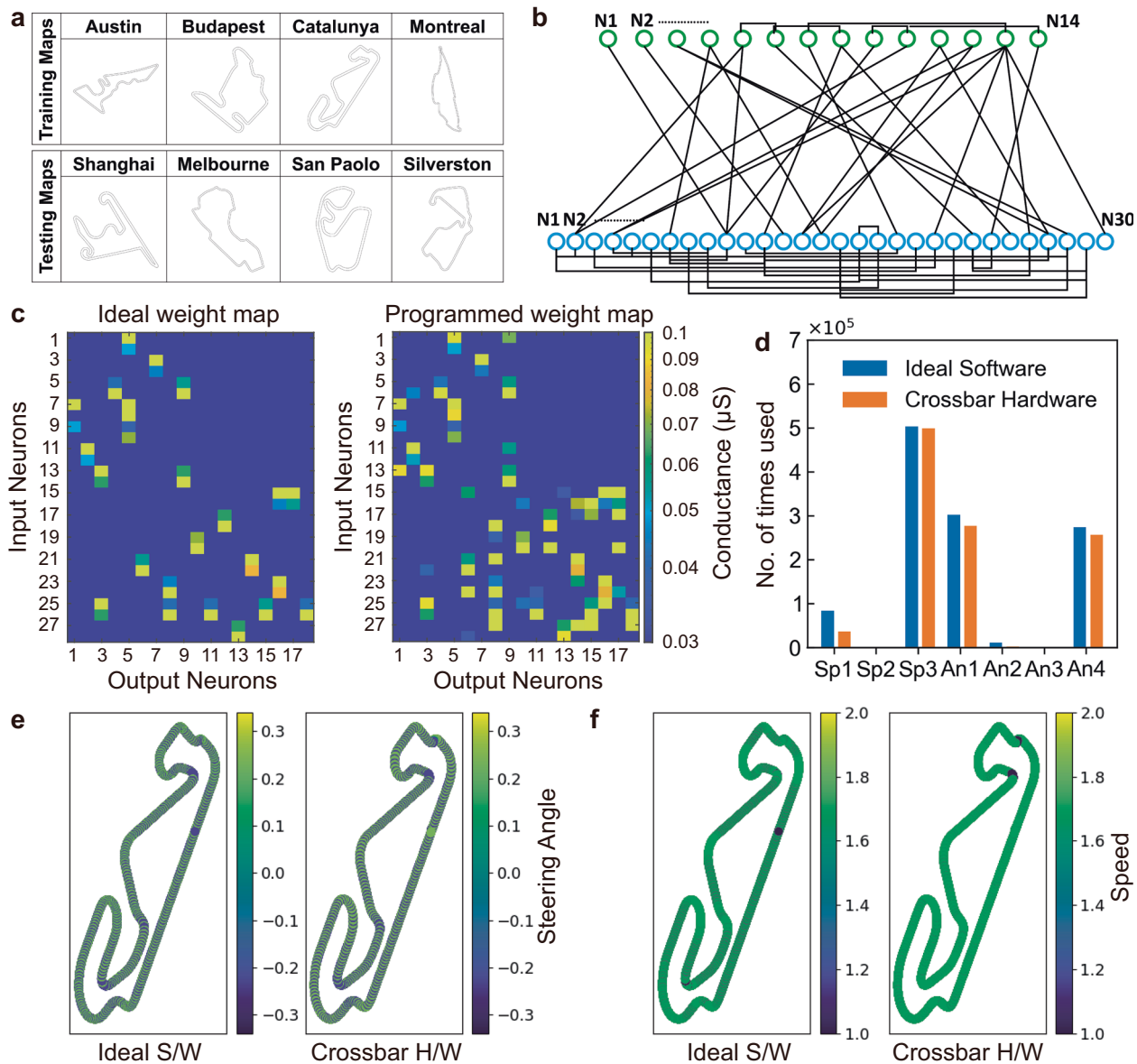


Fig. 6 | Hardware implementation of SNN for a navigation/racing task.

a Examples of training and testing racetracks for navigation tasks. **b** Schematics of trained SNN (14 input/30 output neurons). **c** Weight map comparison between ideal weights and experimentally programmed weights on crossbars using the row-differential encoding. Two 16×16 crossbars were used for weight mapping.

d Number of speed (Sp = 1, 1.6, 1.7) and steering angle (An = -0.23, 0, 0.17, 0.23)

computations across navigation through all fifteen racetracks. Ideal software simulation and crossbar hardware implementation show highly consistent results. (Fitness score: 0.54 (Ideal S/W) vs. 0.43 (Crossbar H/W)). Ideal software vs. crossbar hardware computation of **e** steering angle and **f** speed during testing in the Catalunya map.

deposited with sputtering under the different oxygen partial pressures to induce the V_O into the film (S3: 100 W, $O_2/(O_2+Ar) = 10\%$ /S4: 200 W, $O_2/(O_2+Ar) = 5\%$). Ti (12 nm)/TiN (22 nm)/Ti (12 nm)/Au (200 nm) top electrode was deposited and patterned analogous to the bottom electrode lift-off process. The switching layer was etched away by plasma etching processed with $O_2/CF_4/Ar/BCl_3$ gas chemistry. The Au wire bonding was done using manual west bond ball bonder equipment.

Materials characterization

For structural characterization, high-resolution X-ray scattering measurements (Grazing Incidence X-ray diffraction and X-ray reflection) were conducted using in-house X-ray diffraction (Smartlab XRD, Rigaku). Transmission electron microscopy (TEM)-ready samples were prepared using the in-situ FIB lift-off technique on an FEI Dual Beam FIB/SEM. The samples were capped with sputtered Ir and e-Pt/I-Pt prior to milling. The TEM lamella thickness was ~ 100 nm. The samples were

imaged with a FEI Tecnai TF-20 FEG/TEM operated at 200 kV in bright-field (BF) TEM mode, high-resolution (HR) TEM mode, and high-angle annular dark-field (HAADF) STEM mode. The STEM probe size was 1-2 nm nominal diameter.

Electrical characterization and weight mapping on crossbars

The electrical I-V characteristics of the RRAM devices were measured using a semiconductor analyzer (4155 C, Agilent) and switching matrix (E5250A, Keysight). A pulse generator unit (81110 A, Agilent) and pulse measurement units with remote amplifiers (4200-SCS with 4225-PMU and 4225-RPM, Keithley) were used for the pulse generation and measurements.

The bulk RRAM crossbar arrays were wire-bonded on pin grid arrays and mounted on custom designed printed circuit board (PCB) to map the weights on the arrays. Weight mapping process on the arrays was conducted using connected switching matrix,

semiconductor analyzer, and a pulse generator unit. We implemented an Opal Kelly FPGA Board to demonstrate the voltage sensing scheme⁴⁶. The conductance was calculated by driving WLs to V_{pulse} and measuring the time constant of BL charging. Then the absolute conductance was calculated by the following expression.

$$V_{BL} \approx V_{ref} + \frac{g_i}{\sum_{k=1}^N g_k} V_{pulse}, \text{ for } t \gg \frac{C}{\sum_{k=1}^N g_k} \quad (1)$$

For row differential MVM read-out to obtain expected versus measured results, we took difference between RRAM devices (G^+ and G^-) from two consecutive word-lines (WL^+ and WL^-) on the same bit-line (BL). To perform the read-out operation, the ternary inputs ($X = [-1, 0, 1]$) are assigned to each differential pair. When the input $X_i = 1$, +Vread ($V_{ref} + 0.1V$) is applied to the WL^+ and -Vread ($V_{ref} - 0.1V$) is applied to the WL^- . In the case of $X_i = -1$, -Vread ($V_{ref} - 0.1V$) is applied to the WL^+ and +Vread ($V_{ref} + 0.1V$) is applied to WL^- . If the input $X_i = 0$, then V_{ref} is applied to both WL^+ and WL^- .

The charged voltage on the sampling capacitor is expressed as Eq. (2).

$$V_{row-diff} = V_{ref} + \frac{\sum_i (G_i^+ - G_i^-) \times X_i \times |V_{read} - V_{ref}|}{\sum_i (G_i^+ + G_i^-)} \quad (2)$$

where $i = [1, 2, \dots, 8]$ represents the number of differential pairs and V_{ref} is the pre-charge voltage of sampling capacitor.

The expected MVM values are calculated after inserting the extracted conductance values and the random sequence ternary input vector 'Xi' in Eq. (2). In this case, first we read the total conductance value on the shared/selected BL and then individual conductance value of each RRAM on the same BL. To obtain the total conductance, we activated all the WLs with Vread ($V_{ref} + 0.1V$) and extracted RC time constant of the charged voltage on a known value sampling capacitor at selected BL. After deriving total conductance of the BL, the conductance of each cross point is extracted by applying Vread ($V_{ref} + 0.1V$) on the targeted WL and V_{ref} on the rest of the WLs. When the charged voltage on the sampling capacitor reaches saturation, the measured voltage is proportional to the ratio of individual RRAM conductance to the total conductance:

$$V = V_{ref} + \frac{G_{target}}{G_{total}} |V_{read} - V_{ref}| \quad (3)$$

where $G_{total} = \sum_{i=1}^8 (G_i^+ + G_i^-)$.

On the other hand, to obtain the measured MVM values, we applied a random sequence of ternary input vector 'Xi' to the differential pairs. For every ternary random input vector, we captured the charged voltage on the sampling capacitor using commercial 16-bit resolution successive approximation register analog-to-digital converter (SAR-ADC) (ADS7067, Texas Instruments). We presented these measurement results as expected MVM vs measured MVM which follow the linear trend as shown in paper (Fig. 5g).

Formula-1 track simulation

We leveraged the TENNLab Neuromorphic Framework software framework⁵¹, along with Evolutionary Optimization for Neuromorphic Systems (EONS)⁴⁷ to design a spiking neural network for evaluation in our hardware. The task that we optimized the neural network for was autonomous control of a small-scale autonomous race car. We leveraged the FITenth⁵² simulation environment for training. In this environment, the observations provided to the neural network as input are LIDAR observations from the car, and the actions that can be applied (that are produced as output by the network) are steering angle and speed.

We defined discrete values that the network can choose for steering angles ($[0, -0.01, 0.01, -0.03, 0.03, -0.05, 0.05, -0.07, 0.07, -0.1, 0.1, -0.13, 0.13, -0.15, 0.15, -0.17, 0.17, -0.2, 0.2, -0.23, 0.23, -0.25, 0.25, -0.27, 0.27, -0.3, 0.3, -0.34, 0.34]$) and speed ($[1, 1.1, 1.2, 1.3, 1.4, 1.5, 1.6, 1.7, 1.8, 1.9, 2]$). Two sets of output neurons are created, one for steering angle and one for speed, and within those sets, one for each legal value. At each step of the simulated environment, the car receives as input 10 LIDAR beams, down-selected from the full 960 LIDAR beams by selecting the maximum beam distance in each of ten equal-sized regions of the 960 beams. Then, the network simulates for 50 time steps, and the output neuron that fires most for steering angle corresponds to the selected steering angle value (and similarly for speed). Observations are taken and actions are applied of 2 milliseconds in the simulation. Thus, the network makes decision about steering angle and speed every 2 milliseconds.

Following methods similar to those in ref. 48, we used EONS to optimize the parameters (synaptic weights and neuron thresholds) and structure (number of hidden neurons and connectivity between neurons) of a single spiking neural network. EONS is an evolutionary algorithm-based approach that begins with an initial population of randomly initialized networks. Then, each network is evaluated to determine a training score. These scores are used with tournament selection to preferentially select better-performing networks to serve as parents. Then, new networks are created from those parents through recombination/crossover and random mutations. The new population is then evaluated, and this process is repeated for a fixed number of generations. In this case, we optimized a single network for 200 generations. The training performance of the network that is used to drive the optimization is the average score across five real-world Formula 1 tracks, where the score for each track is the percentage of two laps completed without crashing. The testing score of the network is the average score across fifteen other Formula 1 tracks (i.e., tracks not used during training). In this previous work, we have seen that the networks trained in simulation are frequently able to translate to successfully operate a small-scale physical autonomous car.

Figure 6d-f shows the direct performance comparison between software and hardware crossbar-based implementation using the speed ($Sp = 1, 1.6, 1.7$) and steering angle ($An = -0.23, 0, 0.17, 0.23$) values chosen by the network out of all provided 11 speed values and 29 steering angles. EONS algorithm optimized the structure of the spiking neural network and through the optimization, it determined the most suitable speed and angle values among all the provided speed and angle values needed to perform the task.

Data availability

The data that support the plots and other results of this paper are available from the corresponding author upon request.

Code availability

The software codes used for this study are available from the corresponding author upon request.

References

- Schuman, C. D. et al. Opportunities for neuromorphic computing algorithms and applications. *Nat. Computat. Sci.* **2**, 10–19 (2022).
- Jouppi, N. P. et al. In-datacenter performance analysis of a tensor processing unit. In *Proceedings of the 44th annual international symposium on computer architecture*, 1–12 (Association for Computing Machinery, 2017).
- Keckler, S. W., Dally, W. J., Khailany, B., Garland, M. & Glasco, D. GPUs and the future of parallel computing. *IEEE Micro* **31**, 7–17 (2011).
- Oh, S., Huang, Z., Shi, Y. & Kuzum, D. The impact of resistance drift of phase change memory (PCM) synaptic devices on artificial neural network performance. *IEEE Electron Device Lett.* **40**, 1325–1328 (2019).

5. Shi, Y. et al. Performance prospects of deeply scaled spin-transfer torque magnetic random-access memory for in-memory computing. *IEEE Electron Device Lett.* **41**, 1126–1129 (2020).
6. Shi, Y. et al. Neuroinspired unsupervised learning and pruning with subquantum CBRAM arrays. *Nat. Commun.* **9**, 5312 (2018).
7. Oh, S. et al. Energy-efficient Mott activation neuron for full-hardware implementation of neural networks. *Nat. Nanotechnol.* **16**, 680–687 (2021).
8. Jerry, M. et al. Ferroelectric FET analog synapse for acceleration of deep neural network training. In *2017 IEEE international electron devices meeting (IEDM)*, 6.2. 1–6.2. 4 (IEEE, 2017).
9. Kim, H., Mahmoodi, M., Nili, H. & Strukov, D. B. 4K-memristor analog-grade passive crossbar circuit. *Nat. Commun.* **12**, 5198 (2021).
10. Wang, Q., Wang, X., Lee, S. H., Meng, F.-H. & Lu, W. D. A deep neural network accelerator based on tiled RRAM architecture. In *2019 IEEE international electron devices meeting (IEDM)*, 14.14. 11–14.14. 14 (IEEE, 2019).
11. Schranghamer, T. F., Oberoi, A. & Das, S. Graphene memristive synapses for high precision neuromorphic computing. *Nat. Commun.* **11**, 5474 (2020).
12. Ge, R. et al. Atomistor: nonvolatile resistance switching in atomic sheets of transition metal dichalcogenides. *Nano Lett.* **18**, 434–441 (2018).
13. Seo, S. et al. Artificial van der Waals hybrid synapse and its application to acoustic pattern recognition. *Nat. Commun.* **11**, 3936 (2020).
14. Christensen, D. V. et al. 2022 roadmap on neuromorphic computing and engineering. *Neuromorphic Comput. Eng.* **2**, 022501 (2022).
15. Wan, W. et al. A compute-in-memory chip based on resistive random-access memory. *Nature* **608**, 504–512 (2022).
16. Wan, W. et al. 33.1 A 74 TMACS/W CMOS-RRAM neurosynaptic core with dynamically reconfigurable dataflow and in-situ transposable weights for probabilistic graphical models. In: *2020 IEEE International Solid-State Circuits Conference (ISSCC)*, 498–500 (IEEE, 2020).
17. Raghavan, N. et al. Stochastic variability of vacancy filament configuration in ultra-thin dielectric RRAM and its impact on OFF-state reliability. In: *2013 IEEE International Electron Devices Meeting*, 21.21. 21–21.21. 24 (IEEE, 2013).
18. Kim, S. et al. 4-bit Multilevel Operation in Overshoot Suppressed Al₂O₃/TiO_x Resistive Random-Access Memory Crossbar Array. *Adv. Intell. Syst.* **4**, 2100273 (2022).
19. Rao, M. et al. Thousands of conductance levels in memristors integrated on CMOS. *Nature* **615**, 823–829 (2023).
20. Chen, A. A comprehensive crossbar array model with solutions for line resistance and nonlinear device characteristics. *IEEE Trans. Electron Dev.* **60**, 1318–1326 (2013).
21. Xia, Q. & Yang, J. J. Memristive crossbar arrays for brain-inspired computing. *Nat. Mater.* **18**, 309–323 (2019).
22. Yu, L.-E., Kim, S., Ryu, M.-K., Choi, S.-Y. & Choi, Y.-K. Structure Effects on Resistive Switching of Al/TiO_x/Al Devices for RRAM Applications. *IEEE Electron Device Lett.* **29**, 331–333 (2008).
23. Zhang, H. et al. Understanding the coexistence of two bipolar resistive switching modes with opposite polarity in Pt/TiO₂/Ti/Pt nanosized ReRAM devices. *ACS Appl. Mater. Interfaces* **10**, 29766–29778 (2018).
24. Jacob, K. & Gupta, S. Calciothermic reduction of TiO₂: A diagrammatic assessment of the thermodynamic limit of deoxidation. *JOM* **61**, 56–59 (2009).
25. Kang, M. & Son, J. Off-state current reduction in NbO₂-based selector device by using TiO₂ tunneling barrier as an oxygen scavenger. *Appl. Phys. Lett.* **109**, 202101 (2016).
26. Calka, P. et al. Engineering of the Chemical Reactivity of the Ti/HfO₂ Interface for RRAM: Experiment and Theory. *ACS Appl. Mater. Interfaces* **6**, 5056–5060 (2014).
27. Park, J., Yoon, H., Sim, H., Choi, S.-Y. & Son, J. Accelerated hydrogen diffusion and surface exchange by domain boundaries in epitaxial VO₂ thin films. *ACS Nano* **14**, 2533–2541 (2020).
28. Navickas, E. et al. Fast oxygen exchange and diffusion kinetics of grain boundaries in Sr-doped LaMnO₃ thin films. *Phys. Chem. Chem. Phys.* **17**, 7659–7669 (2015).
29. Padovani, A., Larcher, L., Pirrotta, O., Vandelli, L. & Bersuker, G. Microscopic modeling of HfO_x RRAM operations: From forming to switching. *IEEE Trans. Electron Devices* **62**, 1998–2006 (2015).
30. Kim, M. et al. Filamentary and interface-type memristors based on tantalum oxide for energy-efficient neuromorphic hardware. *ACS Appl. Mater. Interfaces* **14**, 44561–44571 (2022).
31. Fantini, A. et al. Intrinsic switching variability in HfO₂ RRAM. In: *2013 5th IEEE International Memory Workshop*, 30–33 (IEEE, 2013).
32. Lenzlinger, M. & Snow, E. Fowler-Nordheim tunneling into thermally grown SiO₂. *J. Appl. Phys.* **40**, 278–283 (1969).
33. Simmons, J. G. Electric tunnel effect between dissimilar electrodes separated by a thin insulating film. *J. Appl. Phys.* **34**, 2581–2590 (1963).
34. Govoreanu, B. et al. Vacancy-modulated conductive oxide resistive RAM (VMCO-RRAM): An area-scalable switching current, self-compliant, highly nonlinear and wide on/off-window resistive switching cell. In: *2013 IEEE International Electron Devices Meeting*, 10.12. 11–10.12. 14 (IEEE, 2013).
35. Park, J. et al. Conduction mechanism effect on physical unclonable function using Al₂O₃/TiO_x memristors. *Chaos Solitons Fractals* **152**, 111388 (2021).
36. Shi, Y. et al. Integration of Ag-CBRAM crossbars and Mott ReLU neurons for efficient implementation of deep neural networks in hardware. *Neuromorphic Comput. Eng.* **3**, 034007 (2023).
37. Mark, P. & Helfrich, W. Space-charge-limited currents in organic crystals. *J. Appl. Phys.* **33**, 205–215 (1962).
38. Lampert, M. A. Simplified theory of space-charge-limited currents in an insulator with traps. *Phys. Rev.* **103**, 1648 (1956).
39. Lampert, M. A. & Schilling, R. B. *Current injection in solids: The regional approximation method*. 6 (Elsevier, 1970).
40. Waser, R. & Aono, M. Nanoionics-based resistive switching memories. *Nat. Mater.* **6**, 833–840 (2007).
41. Grossi, A. et al. Electrical characterization and modeling of 1T-1R RRAM arrays with amorphous and poly-crystalline HfO₂. *Solid State Electronics* **128**, 187–193 (2017).
42. Wu, Y. et al. Demonstration of a Multi-Level μ A-Range Bulk Switching ReRAM and its Application for Keyword Spotting. In *2022 International Electron Devices Meeting (IEDM)*, 18.14. 11–18.14. 14 (IEDM, 2022).
43. Shi, Y. et al. Adaptive quantization as a device-algorithm co-design approach to improve the performance of in-memory unsupervised learning with SNNs. *IEEE Trans. Electron Devices* **66**, 1722–1728 (2019).
44. Nagel, M., Baalen, M. v., Blankevoort, T. & Welling, M. Data-free quantization through weight equalization and bias correction. In *Proceedings of the IEEE/CVF International Conference on Computer Vision*, 1325–1334 (IEEE, 2019).
45. Gholami, A. et al. *A survey of quantization methods for efficient neural network inference*. (Chapman and Hall/CRC, 2022).
46. Jain, S. et al. A Versatile and Efficient Neuromorphic Platform for Compute-in-Memory with Selector-less Memristive Crossbars. In *2023 IEEE International Symposium on Circuits and Systems (ISCAS)*, 1–4 (IEEE, 2023).
47. Schuman, C. D., Mitchell, J. P., Patton, R. M., Potok, T. E. & Plank, J. S. Evolutionary optimization for neuromorphic systems. In *Proceedings of the 2020 Annual Neuro-Inspired Computational Elements Workshop*, 1–9 (ACM, 2020).
48. Schuman, C. et al. Evolutionary vs imitation learning for neuromorphic control at the edge. *Neuromorphic Comput. Eng.* **2**, 014002 (2022).

49. Grenouillet, L. et al. 16kbit 1T1R OxRAM arrays embedded in 28nm FDSOI technology demonstrating low BER, high endurance, and compatibility with core logic transistors. In *2021 IEEE International Memory Workshop (IMW)*, 1–4 (IEEE, 2021).
50. Nayfeh, A. & El-Atab, N. *Nanomaterials-Based Charge Trapping Memory Devices* (Elsevier, 2020).
51. Plank, J., Schuman, C., Bruer, G., Dean, M. & Rose, G. The TENNLab Exploratory Neuromorphic Computing Framework. *IEEE Lett. Comput. Soc.* **1**, 17–20 (2018).
52. O’Kelly, M., Zheng, H., Karthik, D. & Mangharam, R. F1tenth: An open-source evaluation environment for continuous control and reinforcement learning. In: *Proceedings of Machine Learning Research* 123 (PLMR, 2020).

Acknowledgements

This work was supported by the Office of Naval Research (N000142012405) and the Quantum Materials for Energy Efficient Neuromorphic Computing (Q-MEEN-C), an Energy Frontier Research Center (EFRC), funded by the US Department of Energy, Office of Science, Basic Energy Sciences under award #DE-SC0019273.

Author contributions

This work was conceived by J.P., A.K., and D.K. Fabrication was performed by J.P., Y.Z., and S.O. Electrical characterization and analysis of RRAM devices were performed by J.P., A.K., and Y.Z. Temperature-dependent electrical characterization were performed by J.P., Y.Z., E.Q. and I.K.S. Materials characterization was performed by J.P. Crossbar analysis was performed by J.P., A.K., Y.S., J.-H.K., S.J., G.H., G.C. SNN Hardware implementation were performed by A.L.N and C.D.S. All the authors discussed the results and contributed to the writing of the manuscript. D.K. supervised the work.

Competing interests

The authors declare no competing interests.

Additional information

Supplementary information The online version contains supplementary material available at <https://doi.org/10.1038/s41467-024-46682-1>.

Correspondence and requests for materials should be addressed to Duygu Kuzum.

Peer review information *Nature Communications* thanks Adrian Ionescu, and the other, anonymous, reviewer(s) for their contribution to the peer review of this work. A peer review file is available.

Reprints and permissions information is available at <http://www.nature.com/reprints>

Publisher’s note Springer Nature remains neutral with regard to jurisdictional claims in published maps and institutional affiliations.

Open Access This article is licensed under a Creative Commons Attribution 4.0 International License, which permits use, sharing, adaptation, distribution and reproduction in any medium or format, as long as you give appropriate credit to the original author(s) and the source, provide a link to the Creative Commons licence, and indicate if changes were made. The images or other third party material in this article are included in the article’s Creative Commons licence, unless indicated otherwise in a credit line to the material. If material is not included in the article’s Creative Commons licence and your intended use is not permitted by statutory regulation or exceeds the permitted use, you will need to obtain permission directly from the copyright holder. To view a copy of this licence, visit <http://creativecommons.org/licenses/by/4.0/>.

© The Author(s) 2024